EFFECT OF MOISTURE LEVEL IN PLATE THERMOMETER INSULATION ON THE MEASUREMENT OF INCIDENT RADIANT HEAT FLUX

By

LAHIRU JAYATHUNGA MUDIYANSELAGE

Bachelor of Science in Mechanical Engineering

University of Moratuwa

Colombo, Sri Lanka

2013

Submitted to the Faculty of the
Graduate College of the
Oklahoma State University
in partial fulfillment of
the requirements for
the Degree of
MASTER OF SCIENCE
May, 2020

EFFECT OF MOISTURE LEVEL IN

PLATE THERMOMETER INSULATION ON THE

MEASUREMENT OF

INCIDENT RADIANT HEAT FLUX

Thesis Approved:

Dr. Haejun Park

Thesis Adviser

Dr. Rob Agnew

Dr. Virginia Charter

ACKNOWLEDGMENT

I truly wish to thank all the individuals who have helped and supported me throughout this journey. I wish to extend my sincere appreciation towards Dr. Haejun Park, my thesis advisor for his trust in me with this project, for his excellent mentoring, for his contagious professionalism and for being patient and kind while guiding me in the right direction. His charisma and his dedication towards work fueled my enthusiasm to upgrade myself as a nascent researcher.

I also wish to thank my committee members: Dr. Rob Agnew and Dr. Virginia Charter for their constructive criticism, support, and guidance throughout this pr[oc]ess of pursuing my degree.

I believe it is a privilege to work with such an amazing and supportive bunch of colleagues: Qingtong Liu and Lujia Wang, without their cooperation this journey would have been difficult. In addition to that, I am grateful for the friendship and guidance rendered to me by many other professors, fellow graduate students, and supporting staff. I am so grateful for the support and understanding of my family especially my wife: Bhagya, and my parents.

Name: LAHIRU JAYATHUNGA MUDIYANSELAGE

Date of Degree: MAY, 2020

Title of Study: **EFFECT OF MOISTURE LEVEL IN PLATE THERMOMETER INSULATION ON THE MEASUREMENT OF INCIDENT RADIANT HEAT FLUX**

Major Field: FIRE SAFETY AND EXPLOSION PROTECTION

Abstract: The purpose of the current study was to elucidate the fluctuations of calculated heat fluxes based on two independent conditions of the insulation layers of the plate thermometer (PT). An equation developed using ideal surface temperature was used to calculate the incident radiant heat flux from the PT. A Schmidt-Boelter type radiometer was used in validating calculated incident radiant heat flux from the subjected PT. The effect of changing the microphysical properties of insulation layers upon the temperature was investigated in the first phase of the research. The calculated and measured incident radiant heat fluxes seemed to be overlapping with each other in a preheated PT despite the comparatively wider difference between the same parameters of an unheated PT. The second stage was to evaluate the changes of calculated incident radiant heat flux against the inherent moisture percentages of respective insulation layers. Four moisture percentages were identified as conditions representing distinct climatic conditions in Stillwater, Oklahoma; the moisture percentages are equivalent to wood moisture equivalent (%WME) 0, 45, 65, and 98. The results show that there was no significant difference of incident radiant heat fluxes measured with a radiometer and calculated using PT within 0 to 65 %WME. Further, the noticeable difference between the incident radiant heat flux with 98 %WME was caused due to the significant vaporization energy consumed from the moisture inside the PT insulations. The optimum possible weather condition for the highest %EMC was considered. Accuracy of the measured incident radiant heat flux was checked with the respective %WME values. To conclude, the researchers recommended using preheated PT with any moisture percentage under 65 %WME to obtain accurate enough incident radiant heat flux measurements.

TABLE OF CONTENTS

LIST OF TABLES

Table Page

LIST OF FIGURES

Figure Page

NOMENCLATURE

c_p	Specific heat of Inconel 600 metal plate [kJ/(kg K)]
h	Convective heat transfer coefficient (W/m^2 K)
h_{cont}	Contact correction factor (W/m^2 K)
ρ	Thermal conductivity (W/mC)
L	Length of the plate (m)
$\dot{q}^{n}_{cond}$	Conduction loss (W/m^2)
$\dot{q}^{"}_{cont}$	Contact heat loss (W/m^2)
$\dot{q}^{"}_{conv}$	Convective heat flux (W/m^2)
$\dot{q}^{"}_{HFG}$	Total heat flux of Schmidt-bolter type total flux gauge (W/m^2)
$\dot{q}^{"}_{inc}$	Incident heat flux (W/m^2)
ε_{PT}	Incident radiation heat flux (W/m^2)
$\dot{q}^{"}_{re-rad}$	Re-radiation (W/m^2)
$\dot{q}^{"}_{stored}$	Heat energy stored (W/m^2)
R_a	Rayleigh number
T_∞	Ambient temperature (K)
T_g	Gas temperature (K)
T_s	Measured surface temperature of Inconel 600 metal plate (K)
$T_{s-ideal}$	Ideal surface temperature of Inconel 600 metal plate (K)
t	Time (s)
ε_{HFG}	Surface emissivity of Schmidt-bolter type total heat flux gauge
ε_{PT}	Surface emissivity of PT
ρ	Density of Inconel 600 metal plate (kg/m^3)
ρ_{ins}	Density of insulation (kg/m^3)
σ	Stefan-Boltzmann constant [W/(m^2 K^4)]
δ	Thickness of Inconel 600 metal plate (m)

CHAPTER I

INTRODUCTION

According to the National Fire Protection Association (NFPA), fire is "A rapid oxidation process, which is a chemical reaction resulting in the evolution of light and heavy in varying intensities" (*NFPA 921 (2011)*, 2013). The study of fire dynamics explains three methods of energy transfer during a fire: conduction, convection, and radiation (Hurley, 2016). Conduction is a mode of energy transfer from a point of high temperature to a point of low temperature across a medium. Convection effects when the motion of particles along the temperature gradient transfers heat from the heat source to a target; wherein fluid acts as an intermediary. Radiation does not require a medium to be transported between the source and the target. This phenomenon explains the energy transfer utilizing electromagnetic waves or photons. Building upon these phenomena, the two most important modes of heat transfer during a fire scenario were determined as two of the aforementioned methods: radiation and convection.

The heat transfer in a fire scenario significantly affects the strength and performance of surrounding structures. The weakening of load-bearing structures such as beams, columns, and slabs as well as non-load bearing structures such as partition walls, and floors are

unavoidable in a compartment fire. Numerous researchers have suggested that the effects of fire destabilize the resistance of various structures against fire. For instance, altering the mechanical properties such as strength and stiffness of a material can lead to a weakening of even the noncombustible materials (Hurley, 2016).

Determining the amount of heat flux a surface of interest is exposed in a thermal interaction between a heat source and its surroundings is vital in practical fire conditions. The commercially available tools traditionally being used to measure total heat flux by the fire safety researchers are Schmidt-Boelter gauge and Gardon gauge (Ochs *et al*., 2013). The popularity of these gauges is ascribed to the prompt thermal response and accurate calibration procedure of the tools (Hukseflux SBG01 user manual v1208, 2011). Both these gauges are water-cooled to provide a good heat sink by continuously removing absorbed heat. Resulting condensation of water and soot deposition can lead to erroneous heat flux calculations. In addition to that, using such gauges can be very inconvenient in real-life scenarios as well as during fire safety testing in wildlands and funnels where continuous water supply is not available (ASTM E3057-19, 2019).

As the need for a more robust and less expensive alternative to the water-cooled gauges rose, the researchers started developing a device called plate thermometer (PT) to measure temperatures in fire resistance tests. The temperature measured using the PT was subsequently used to calculate the heat flux. PT consists of a metal plate, a thermocouple connected to this plate and an insulation layer to minimize the heat loss. The objective of this study is to determine the fluctuation of calculated incident radiant heat flux of the PT along with the moisture content (%MC) of the insulation layers.

CHAPTER II

BACKGROUND

2.1 Heat Transfer Basics

Thermal engineering explains general heat transfer as “thermal energy in transit due to spatial temperature difference” with a focus on heat transport, exchange, and redistribution. Heat transfer will occur only when there is a driving force and a temperature difference within a medium or in between two or several media. As explained in the introduction, there are three prime heat transfer modes, namely conduction, convection, and radiation (Bahrami, 2013).

- Conduction

Molecular agitation within a material can contribute to heat transfer without necessarily any motion of the material as a whole. This phenomenon is called conduction. The molecules with a higher speed at the hot end of material colliding with the slower molecules transfer energy towards the colder end. Thermal conductivity is an inherent property of any material that, defines its ability to conduct heat. According to Fourier’s law of heat transfer, the heat transfer rate is directly proportional to the temperature gradient across the object

and is a function of thermal conductivity. The equation for one-dimensional heat transfer is expressed as Eq. (1) (FPST handbook).

$$q''_{conduction} = -k\frac{dT}{dx} \tag{1}$$

- Convection

Convection is a mode of heat transfer with the mass movement of fluid. There should be a solid surface and moving fluid flow, in different temperatures to occur the convection. The temperature difference between the surface and the fluid, and the thermal conductivity of the fluid, convective heat transfer coefficient, are the main controlling factors of the convection in the thermal environment. Convective heat transfer can be subdivided into two categories, depending on the source of fluid movement: 'natural convection' when there is no involvement of external force and 'forced convection' when an external force such as wind is present to induce the motion of the fluid. Given below in Eq. (2), is the technical way of calculating convective heat transfer (FPST handbook).

$$q''_{convection} = h(T_s - T_\infty) \tag{2}$$

- Radiation

The principal mode of heat transfer during a fire scenario is radiation. This distinct method of energy transfer enables two or more spatially separate objects with different temperatures to transfer heat. Electromagnetic wave theory explains the nature of thermal radiation very well using the Stefan-Boltzman Law given below in Eq. (3) (FPST handbook).

$$q''_{radiation} = \varepsilon\sigma T_s^4 \tag{3}$$

2.2 Cone Calorimeter

The cone calorimeter was developed as an apparatus to determine the heat release rate and incident radiant heat fluxes from fire experiments. The physical appearance of the cone calorimeter is shown in Figure 1. Despite other purposes, the main purpose of the cone calorimeter is to assess the level of flammability of materials, used in fire safety engineering. The conical-shaped cone heater in the cone calorimeter emits the heat upon the material sample placed under the cone heater. The incident radiant heat flux from the cone heater can be changed with the cone heater temperature and then use heat flux gauges to measure the incident radiant heat fluxes form the cone heater. Likewise, the incident radiant heat flux received by the material under the cone heater can be determined (Kang *et al.*, 2019). The maximum heat flux delivered to the specimen from the cone heater is 100 kW/m^2 (Cone calorimeter,2019).

Figure 1: Cone calorimeter

2.3 Industrial Heat Flux Gauges

Gardon and Schmidt-Boelter gauge are the two main commercially available heat flux gauges. The method adopted by Gardon gauge to measure the heat flux is the temperature

difference developed between the center of the metallic foil and its peripheral junction attached to the water cooling outer surface of the gauge. Thermally stable material connects the sensing surface and the gauge body. Schmidt-Boelter type gauge uses an electrical signal generated by the temperature difference between the ends of this thermally stable material. Previous research suggests that the surface temperature is effectively validated when it is closer to the cooling water temperature (Robertson & Ohlemiller, 1995). Both these gauges are identical in physical appearance but differ in sensor technology used. Gardon gauge uses a thermopile with only two joints whereas Schmidt-Boelter gauge uses multi-junction thermopiles.

This study uses the Schmidt-Boelter gauge due to significant advantages such as the results being more sensitive and linear, lesser coil temperature leading to a different reaction to convection, and the less grounding errors due to the electrically insulated arrangement (Hukseflux SBG01 user manual v1208, 2011). Nevertheless, soot deposition, differences between the measuring and calibration environment, and possible heat losses from the measuring surface can result in uncertainties of the measurements (Mohammed *et al.*, 2016; Nakos, 2005). The major constraint in using these devices apart from the cost is the requirement of cooling water supply. This is a tough requirement to be met in a real fire situation, as the supply of water is not guaranteed at every location.

Schmidt-Boelter water-cooled gauge has two main demonstrations, one is the "water-cooled total heat flux gauge" (WCTHG), and another called "water-cooled radiometer" (WCRM) shown in. WCRM is a heat flux gauge modified by attaching an optical filter in front of the sensing surface (Nakos, 2010). This filter, ideally made of sapphire, blocks the convection heat flux but absorbs a significant amount of radiation from the heat source.

Therefore, the convection contribution to the sensing surface is negligible. WCTHG is capable of measuring both radiation and convection heat flux while the WCRM measures only the radiation heat flux. These Schmidt-Boelter gauges can measure heat flux up to 200 kW/m^2 and a temperature of 1100^{o}C. The sensing surface of the gauge is painted with black paint by default. This paint offers good directional response and improves the absorptivity to 0.95 (Hukseflux SBG01 user manual v1208, 2011). These devices have a standardized calibration procedure, hence approved to be used in fire experiments. Considering the validity of the Schmidt-Boelter gauge, its readings were used as reference values in this study.

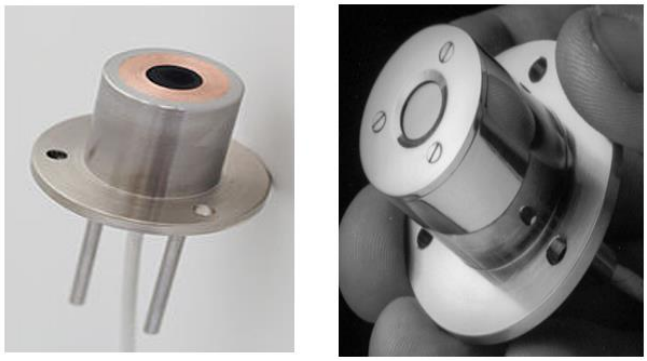

Figure 2: Schmidt-Boelter type Total heat flux gauge and Radiometer

The sum of the net heat flux of convection and radiation is the "total heat flux" (q_{HFG}). The precise value for heat flux measurements can be expected by restricting the re-radiation and optimizing the convection contribution. A technique to reduce the re-radiation is by reducing the measuring surface temperature; external cooling water supply with a temperature range of 20^{o}C – 80^{o}C affirms this requirement. The resulting low temperature not only directly reduces the re-radiation but also maximizes the convection contribution. This recognizable convection is caused by the high-temperature gradient generated

between the surface and the high temperature of the surrounding. This results in recognizable convection on heat flux gauge. The equation for the total heat flux in a thermal environment having both radiation and convection is illustrated in the Eq. (4) below.

$$\dot{q}''_{HFG} = \varepsilon_{HFG}\dot{q}''_{inc-rad} + h(T_g - T_\infty) - \varepsilon_{HFG}\sigma T_\infty^4 \quad (4)$$

Moreover, in a hypothetical situation, wherein the equipment is kept in a thermal environment with ambient temperature conditions, the temperature difference between the front surface and the surroundings becomes negligible. Thereupon, the convection turns out to be negligible as well. Hence, the WCTHG has presented a radiation only condition and the Eq. (5) below can be used to measure total heat flux upon such a situation.

$$\dot{q}''_{HFG} = \varepsilon_{HFG}\dot{q}''_{inc-rad} - \varepsilon_{HFG}\sigma T_\infty^4 \quad (5)$$

These commercial gauges have been validated numerously over the last few decades. In addition to that, they have been optimized to measure the total heat flux in fire situations. However, the major flaw of WCTHGs, requiring a water source for functioning is hindering the usability of these gauges in real-life situations. The researchers are looking into alternatives to measure the total heat flux in real fire situations and the development of the PT is considered a major leap forward, towards achieving this goal.

2.4 Standard Plate Thermometer

The plate thermometer was initially designed to measure the thermal exposures in the fire resistance furnaces as per ISO 834-1(International Organization for Standardization) and EN 1363 (European Standard). Since then, it has been used to measure heat exposures of objects in fire scenarios. Undoubtedly, PT has several advantages over commercial gauges:

simplified design, robustness, and low manufacturing cost compared to other industrial gauges. Moreover, PT is capable of measuring incident radiant heat flux in thermal environments without needing a water supply attesting the convenience of being used in real fire scenarios (Häggkvist, 2009; Häggkvist *et al*., 2013).

The standard PT design consists of a 0.7mm x 100mm x 100mm Nickel alloy plate, folded around a 10-mm-thick organic insulation material (density of 280 +- 30 kg/m^3). The surface temperature of the Inconel alloy plate is measured by the Type K thermocouple welded to its geometric center (Häggkvist, 2009). Perfect insulation is assumed for the standard PT ensuring a negligible heat loss from the insulation layer. Lumped heat analysis of the Inconel alloy plate should be performed to determine whether the temperature gradient across the thickness of the plate remains relatively low.

Incident radiant heat flux calculations by PT showed optimum results when the temperature of the metal plate and the insulation layer are close to each other as in steady-state conditions (Häggkvist *et al*., 2013). Conversely, the incident radiant heat flux calculated from the PT is less than the measured value of the WCTHG in a transient period when the temperature difference between the inconel plate and the insulation layer is high. The reason is identified as the significant amount of heat loss from the insulation layer when heating up, usually not noticeable in surrounding with ambient temperature. A schematic diagram of the standard PT is shown in Figure 3.

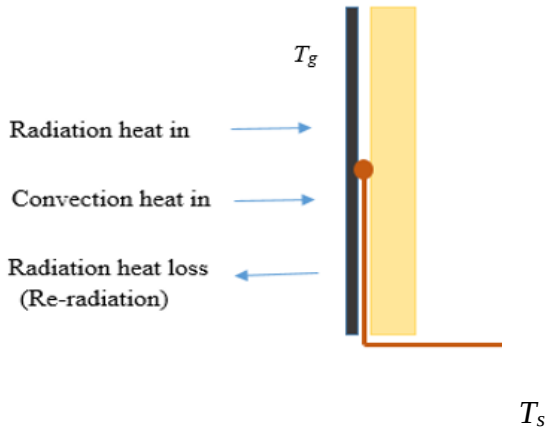

Figure 3: Energy balance of a standard PT

To represent the heat flux measurements of the PT in a mixed thermal environment, heat balance equation; Eq. (6), can be derived by assuming the nickel plate as the control volume.

$$\rho c_p \delta \frac{dT_s}{dt} = \varepsilon_{PT} \dot{q}^{"}_{inc-rad} + h(T_g - T_s) - \varepsilon_{PT} \sigma T_s^4 \tag{6}$$

General clarifications for the phases mentioned above as follows,

$\rho c_p \delta \frac{dT_s}{dt}$ = Heat stored in the Inconel alloy plate (W/m^2)

$\varepsilon_{PT} \dot{q}^{"}_{inc-rad}$ = Radiation heat flux received by the PT (W/m^2)

$h(T_g - T_s)$ = Convection heat flux received by the PT (W/m^2)

$\varepsilon_{PT} \sigma T_s^4$ = Re-radiation from the Inconel alloy plate (W/m^2)

Rearranging above equations, incident radiant heat flux can be expressed as in Eq. (7).

$$\dot{q}^{"}_{inc-rad} = \frac{1}{\varepsilon_{PT}} (\rho c_p \delta \frac{dT_s}{dt} - h(T_g - T_s) + \varepsilon_{PT} \sigma T_s^4) \tag{7}$$

Using the above equation, the incident radiant heat flux can be calculated using the PT, given that other variables are already been determined. The effect on the incident radiant heat flux from the microphysical bonds in the insulations of the PT and the moisture level of the insulation layers were observed in this experiment.

2.5 Effects on Moisture Content to Heat Transfer

2.5.1 Moisture Content Calculation

The moisture content or water content is the indicator of the level of water that rests inside a solid material. Solid materials have porosities, cavities in different amounts that allow water molecules to flow inside the material. The definition of the moisture content or moisture percentage is the ratio between the water mass in a certain volume and the mass of solid in that same volume (UC Merced Engineering, 2002). There are two ways to determine the moisture content in the solid: dry basis moisture content and wet basis moisture content. The respective equations are shown in Eq. (8) and Eq. (9)

$$\%MC_{material\ A} = \frac{concentration_{moisture}\ [\frac{g}{cm^3}]}{density_{materialA}\ [\frac{g}{cm^3}]} \times 100 \tag{8}$$

$$\%MC_{material\ A} = \frac{concentration_{moisture}\ [\frac{g}{cm^3}]}{concentration_{moisture}\ [\frac{g}{cm^3}] + density_{materialA}\ [\frac{g}{cm^3}]} \times 100 \tag{9}$$

Wet basis moisture content is generally used in agriculture, food industry, wood biomass industry, etc. as it represents the moisture content respect to the final product including the moisture. Dry moisture content is used for the industries where moisture is lost and gained such as solid wood products, particle boards, panel boards, etc. (Govett *et al.*, 2019;

Introduction to moisture content determination, Purdue University, 2019). This study uses dry moisture content since the study revolves around determining the moisture content of a solid, such as ceramic fiber insulators.

2.5.2 Meters to Measure Moisture Content

There are several types of moisture meters used at present: conduction type (resistance type), capacitance type, an infrared type, etc. (Ahmed, 2006). Reliability, ability to measure moisture content inside the material, easiness of handling, and low cost are some advantages of conductive and capacitance meters over the others. Conduction type meters consist of two pins that need penetrating the material. These pins can be found in different lengths as either insulated or non-insulted. These types of moisture meters use direct current conductance and resistance between the two pins to measure the moisture content of the material. More moisture leads to more conductance through the pins. The next type is the capacitance-type moisture meters. These are non-destructive meters and more sensible to surface moisture conditions (Ahmed, 2006). These meters work according to the electromagnetic technology as it emits and receives electrical waves from the sensor pad located at the bottom of the device. The amount of water residing in the material manipulates the electrical signal by evaluating the received signal.

The pin-type moisture probe in the thermo-hygrometer (OMEGA™ RH 700) shown in Figure 4, was used to measure the moisture percentage inside the insulation layers of the PT; the measurement was given with unit, "Wood Moisture Equivalent" percentage (%WME). %WME is the moisture content that would be measured if the material were wood. The meter measures the actual moisture content in wood but conversion will be needed when it is being used to measure the moisture content of a material other than wood.

In hard materials such as wood, concrete, etc. the meter gives the surface moisture content due to the difficulty of the pins to reach further from the surface. For the softer materials such as soil, paper, etc. the meter reflects the average moisture level in between the surface and penetration level (OMEGA user's guide, 2019). The actual moisture percentage of the material measured using the meter can be derived as follows.

The relationship between the %WME and moisture condition can be written as follows using dry basis moisture content method Eq. (10) (Appendix A). Combining Eq. (10) with Eq. (8) above for the dry basis moisture content, the correlation in Eq. (11) can be derived.

$$\%WME = \frac{concentration_{moisture}\ [\frac{g}{cm^3}]}{density_{wood}\ [\frac{g}{cm^3}]} \times 100 \tag{10}$$

$$\%MC_{material\ A} = \frac{density_{wood}\ \left(g/cm^3\right)}{density_{material\ A}\ \left(g/cm^3\right)} \times \%WME \tag{11}$$

Figure 4: Thermo-hygrometer

2.5.3 Relative Humidity

The other relatively similar term to explain the moisture content, that describes the moisture percentage in a gaseous volume, is the relative humidity (RH). The RH is the ratio

of the actual water vapor mass per unit area (density) and the saturation vapor density; in other words, the ratio of the actual and the saturation water vapor pressure in a volume (Arther & Saffer, 2015; Lawrence, 2005). The equations for the RH as in Eq. (12).

$$RH = \frac{density_{actual\ vapor}[\frac{g}{cm^3}]}{density_{saturated\ vapor}[\frac{g}{cm^3}]} \times 100 \quad or \quad RH = \frac{pressure_{actual\ vapor}[Pa]}{pressure_{saturated\ vapor}[Pa]} \times 100 \tag{12}$$

The main difference between the moisture percentage and the RH is the phase of the substance, which it applies. RH relates to the water vapor and it is the gaseous phase of the water. Water vapor cannot remain inside the porosities of solid materials as it gets condensed due to low temperatures when passes through the boundary (Condensation Fact Sheet, 2019). Accordingly, only water molecules in liquid phase rest inside the material that allows measuring the moisture content in a solid, but not RH.

Moisture in materials can control the internal physical properties of the material such as thermal conductivity, temperature, and density. When moisture fills the empty spaces of insulation material, the overall moisture content increases. The amount of water absorbed into a certain material depends on the RH and the moisture percentage of the environment. Water is a better conductor than air and several studies have been conducted to validate this phenomenon (LEARN London Metropolitan University, 2004).

Hedlin researched to observe the variations of the heat flow through the roof insulation with moisture content. Moisture content was selected as 1% to represent a summer day and higher moisture levels to get the comparison value. The insulation layer with controlled moisture percentage was placed on top of the roof; heat flow through the insulation layer

was measured using heat flux transducers. The transfer formula to determine the heat flux through the insulation layer is shown below in Eq. (13).

$$J_0Q_0 = I_0TT_0 + I_1TT_1 + I_2TT_2 + J_1Q_1 + J_2Q_2 + K_0TB_0 + K_1TB_1 + K_2TB_2 \quad (13)$$

where,

J_0 = 1

Q = Heat flux (kW/m^2)

The results showed the different temperatures and heat flux values for each selected moisture conditions. Researchers assumed that the reason for the results was due to two reasons: the moisture evaporated from the warm surface of the insulation and condensing at the cold surface upon the energy transfer (Hedlin, 1988). Further, the study showed a noticeable difference in the heat flux measurements of the insulation in different moisture conditions.

Kočí studied the changes in the thermal conductivity and specific heat capacity with the moisture content in porous building materials. The specimens included plasters, thermal insulation boards, etc. After analyzing the results, researchers concluded that the increasing moisture condition harms the thermal properties and energy balance of the building envelope (Kočí *et al.*, 2017).

2.5.4 Equilibrium Moisture Content

Humidity and temperature are the two main atmospheric factors that affect the internal moisture level of any material. Once the porous material is exposed to a humid

environment, the material absorbs the moisture from the environment. Getting the help of the stable surrounding environment, the moisture content inside the material will come to an equilibrium with the environment moisture level (Mitchell, 2017). This moisture content is known as the "Equilibrium Moisture Content" (%EMC) as in Eq. (14) follows (Hailwood & Horrobin, 1946; Mitchell, 2017).

$$EMC = \frac{1800}{W}\left(\frac{Kh}{1-Kh} + \frac{K_1Kh + 2K_1K_2K^2h^2}{1 + K_1Kh + K_1K_2K^2h^2}\right) \tag{14}$$

where,

$W = 330 + (4.52E - 1)T + (4.15E - 3)T^2$

$K = 0.79 + (4.63E - 4)T - (8.44E - 7)T^2$

$K_1 = 6.34 + (7.75E - 4)T - (9.35E - 5)T^2$

$K_2 = 1.09 + (2.84E - 2)T - (9.04E - 5)T^2$

$h = RH$ [%]

T=*dry bulb temperature* [F]

The value of %EMC is generally determined for wood (Simpson, 1998). It can be utilized to determine the maximum possible %WME in the other material types as well. For instance, despite an artificially generated environment, the maximum %WME value which can be achieved by wood is less than %EMC in the given temperature and RH. However, the moisture content percentage in other materials can vary according to the %WME and density ratio between the wood and the material. Typical moisture content percentage values for generic building materials calculated using the %WME are given in Table 1 below. Dry basis moisture method is used to convert %WME to the moisture content in the respective material (appendix A)

Table 1: Equilibrium moisture content - percentage guidance values (source:https://www.pcwi.com.au/protimeter-wme-emc-tables/)

Environment or material condition	RH %	Generic wood	Generic plaster	Generic brick	Generic cement	Generic sand	Generic concrete	%WME
Safe air dry	25	6						6
	30	7						7
	35	8						8
	40	9						9
	45	10						10
	50	11						11
	55	12				4.7	3.9	12
	60	13				5.1	4.2	13
	65	14	0.1	1.0	1.5	5.5	4.5	14
	70	15	0.2	1.3	2.0	5.9	4.8	15
At risk	75	17	0.4	1.6	3.0	6.4	5.2	17
	80	18	0.6	2.4	4.0	6.8	5.4	18
Damp	85	20	1.0	3.0	5.0	7.3	5.7	20
	90	23	1.5	4.0	6.0	8.0	6.0	23
	95	26	2.2	5.5	7.7	9.0	7.0	26
	100							27

The above table shows a notable difference between the %WME and moisture content in the material. To calculate the moisture content of any given material, it is required to know the density or the mass of that material and use Eq. (8) mentioned in the above section.

Understanding the variation of the %EMC in the given environmental condition is important to get a measurement about the maximum moisture level which wood can bear

in that environment. The %EMC in steady-state environmental conditions was plotted against increasing RH at 27 F and is given in Figure 5 (selected temperature 27F) for that purpose. It shows that the range of %EMC generally falls between 0% and 30% in any given environment.

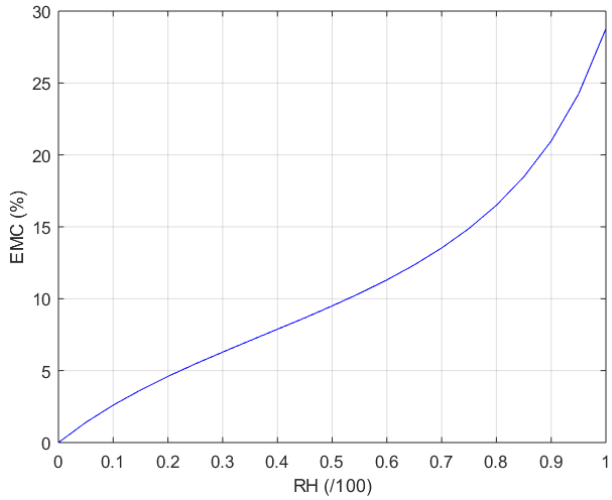

Figure 5: %EMC variation with the RH (at 27 F)

2.6 Design of Plate Thermometer

The design of PT used by Shen in their study was adopted for this research; the model is displayed in Figure 6 (Shen *et al.*, 2019). The design consists of a 25.4 mm x 25.4 mm x 0.584 mm Inconel 600 metal plate, and two layers of ceramic fiber insulation pads bounded with cement board. The Inconel alloy 600 has a density of 8240 kg/m^3 and specific heat capacity of 444 J/kg K. First, 6.35 mm thick insulation pad placed closer to the Inconel plate (Kaowool®PM, Lynn manufacturing, Inc.) and 12.7 mm thick second insulation pad was placed after the first insulation pad (Kaowool®M, Morgan advanced material). 6.35 mm thick, cement board was the last layer of the PT as two thin mechanical wires bind all the layers together. The 'Type K', 24 gauge (0.511 mm) thermocouple was responsible for

measuring the front surface temperature of the plate given that the lumped heat capacitance analysis is valid (Appendix B). The thermocouple was welded to the geometric center of the unexposed surface of the Inconel plate. Another Type K thermocouple was inserted in between the two insulation boards to measure the back surface temperature (T_b) of the first insulation board. The actual image of the PT is shown in Figure 6 and a schematic diagram showing the placement of thermocouples is given in Figure 7.

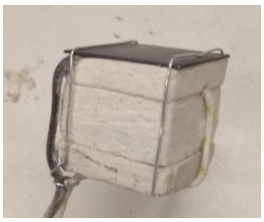

Figure 6: Illustration of the PT new design

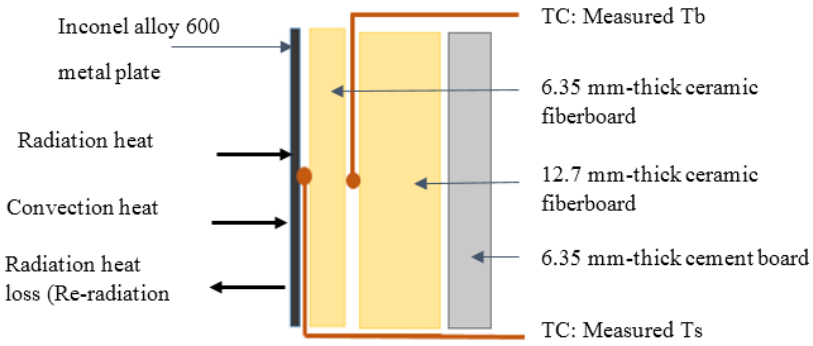

Figure 7: Heat balance of the PT [new design]

The main alteration of this PT design in comparison to the standard design is the reduced size of the overall PT, a feature shared with other commercially available heat flux gauges. Because of reduced dimensions of the Inconel plate, it showed high thermal conductivity and low thermal mass. Furthermore, this results in a very small 'Biot number' (< 0.1) in most fire conditions. A Biot number less than 0.1 suggests that there is a uniform temperature distribution throughout the metal plate in addition to a negligible temperature

gradient. Further, the heat loss from the sides of the Inconel alloy plate can be ignored due to the low thickness. This thermal behavior makes it easy to quantify the heat store inside the PT in transient temperature conditions. As a result, this new plate design is capable of reacting faster under certain fire scenarios and indeed a major advantage of thinner plate design.

To protect the Inconel alloy surface from the oxidative damage at high temperature, the alloy surface is painted with a high-temperature silicon-based paint (Rust-Oleum) in black color. The high-temperature paint used in the current study has been trialed to stand the heat, as high as 1366 K. The black surfaces increase the emissivity of metal surfaces and that varies from zero to one. An assumption was made after logically comparing the standards of the current study with previous research conducted; thereby, the emissivity of PT was determined as 0.85 for this research. The novel PT design absorbs a considerably high amount of heat generated from the fire source due to high emissivity. The measured surface temperature increases proportionally with high absorption.

Another addition to the existing PT design is thick insulation pad layers. As mentioned earlier, the first insulation layer of the new design is lower in thickness, width and length than that of the standard PT. Existing studies provide evidence that reduced thickness facilitates one-dimensional heat transfer only. The thicker second insulation layer further restricts the heat loss from the insulation layers. Therefore, both insulation layers act collectively to reduce the overall heat loss from the Inconel metal plate to the environment.

The assumptions were made as there was no heat loss in PT and occur only a single-sided (1-D) heat transmission from the Inconel alloy plate to the insulation layer. The reading of the second thermocouple, inserted between the two insulation layers, can be used to

calculate the front surface temperature (T_0) of the first insulation pad using the inverse heat conduction method. Considering all the optimized physical properties of the new PT, the heat balance equation for the Inconel alloy plate can be written as follows according to Eq. (15).

$$\rho c_p \delta \frac{dT_s}{dt} = \varepsilon_{PT} \dot{q}''_{inc-rad} - h(T_s - T_g) - \varepsilon_{PT} \sigma T_s^4 - h_{cont}(T_s - T_0) \quad (15)$$

Considering the structure of ceramic fiber insulation, vacuum molding of fiber slurry is the method used to fabricate the highly porous fibrous ceramic. The block of ceramic fiber used as insulation layers is a bird-nest-like structure comprised of a random network of ceramic fiber filled with air. The properties of the ceramic fiber material used as the insulation layers in the new design of PT are compiled in Table 2 below (Thermal ceramics, 2019).

Table 2: Properties of insulation layer materials

Properties	Kaowool PM	Kaowool M
Normal density, PCF	15	17
Maximum temperature rating, ^{0}F	2300	2300
Thermal conductivity, 500/1000 ^{0}F (BTU/hr.ft^2.F)	0.40/ 0.59	0.47/ 0.71

According to a few previously conducted researches, the thermal and mechanical properties of this porous material heavily depends on the bonding between the fibers or the microphysical structure. As per the table above and as proven by numerous researches, the thermal conductivity of this material increases with increasing temperature. The two products utilized in this study: Kaowool®PM and Kaowool®M are the two products that have the lowest nominal density. Sun and his group of researchers have elaborated on the

relationship between porosity, density, and thermal conductivity. As the porosity goes up, the density goes down and it correlates to the increasing thermal conductivity. That affirms the usefulness of Kaowool®PM and Kaowool®M as insulation material (Sun *et al*., 2014).

CHAPTER III

METHODS

3.1 Ideal Surface Temperature

The technique proposed by several previous studies to calculate the ideal surface temperature was used for this study. As defined, the ideal surface temperature is the temperature, the PT should reach in a perfectly insulated condition (Shen *et al.*, 2019). At first, researchers tried to introduce additional terms to the heat balance equations to compensate for the heat losses from the surface (Häggkvist *et al.*, 2013; Ingason & Wickström, 2007). Regardless of the heat loss, researchers of the current study introduced a new temperature term to compensate for the heat losses associated with the PT measurements. The basis of this postulate is that the ideal surface temperature of the Inconel alloy plate correlates the measured surface temperature of the plate given that consistent complete insulation is provided. All causes mentioned below were taken into consideration when developing this correlation, such as heat loss from the metal plate to insulation pad, conduction heat loss, uncertainty factors such as thermocouple wire heating,

and variation of metal thermal properties, etc. Consequently, the calculated ideal surface temperature is always higher than the measured surface temperature as it has to compensate for the heat loss as well. Energy balanced equation can be modified by introducing the ideal surface temperature and can be written as Eq. (16),

$$\rho c_p \delta \frac{dT_{s-ideal}}{dt} = \varepsilon_{PT} \dot{q}_{inc-rad} - \varepsilon_{PT} \sigma T_{s-ideal}^4 - h(T_{s-ideal} - T_g) \tag{16}$$

Another existing concept, 'adiabatic surface temperature', describes the surface temperature in a perfectly insulated condition. According to the definition of "adiabatic surface temperature", the summation of net convection and the net radiation is equal to zero. The heat balance equation for the adiabatic surface temperature is shown in Eq. (17).

$$0 = \varepsilon_{PT} \dot{q}^{"}_{inc-rad} - \varepsilon_{PT} \sigma T_{AST}^4 - h(T_{AST} - T_g) \tag{17}$$

However, both these temperature figures are expected to be equal in steady-state conditions. The temperature gradient in Eq. (15) is considered zero in the steady-state condition. Hence, the steady-state condition can be utilized to develop a correlation between measured and ideal surface temperatures using the process of calibration.

3.2 Experimental Setup

The purpose of this study is to understand the fluctuations of incident radiant heat flux using PT in different microphysical properties and different moisture conditions. Initially, the PT was exposed to gradually increasing temperature; it was anticipated that undergoing this procedure the chemical bonds between the molecules would alter. As the next step, the influence of atmospheric properties on the calculated incident radiant heat flux was

monitored. The PT was configured differently to represent different atmospheric weather conditions essentially by manipulating the moisture level of insulation layers.

The PT design, elaborated in the previous chapter was used for this study. Inconel alloy plate, two layers of insulation layers, and the cement fiberboard were brand new, unheated supplies. Hence, the chemical bonds of these materials were considered as alive. The unheated PT and the water-cooled Schmidt-Boelter gauges were installed under the cone calorimeter heater to determine the incident radiant heat flux.

As explained earlier, the PT underwent initial preparation and exposed to gradually increasing temperature, starting from 200^{o}C heated up until 900^{o}C in 100^{o}C increments. As a result of this increased internal temperature, the microphysical properties of insulation material have changed non-reversibly (Kourtides *et al*., 1988). Further, it was assumed that the properties of the insulation layers completely alter with the changing microphysical properties. Changing properties of the insulation layer can be determined by the thermocouple temperatures. To test for this assumption, researchers compared the measured incident radiant heat fluxes of an unheated PT against a preheated PT.

As the next phase of the research, incident radiant heat flux measurements were obtained by exposing the preheated PT to a representation of a series of weather conditions. The climatic data were gathered using the mesonet climatological data summary for the location Stillwater, Oklahoma. The researchers determined levels of Wood Moisture Equivalent (%WME) percentages to represent the aforementioned weather conditions. The four moisture levels identified for this study were 0, 45, 65, and 98 %WME. PTs were undergone in different processes to imitate these selected moisture levels inside its insulation layers. Those processes are described as follows.

- 0 %WME (possible minimum humidity)

The PT was dried in a furnace (Thermolyne, ThermoScientific) at 60^{o}C until the moisture content of the insulation layers reached 0 %WME. The furnace used to dry the insulation layer is shown in Figure 8 below. Upon reaching the desired moisture percentage due to the evaporation of moisture, the PT was sealed in a zipper-lock bag ensuring no air or moisture trapped inside the bag. The dried PT and the WCRM were positioned under the cone calorimeter heater to measure the surface temperature and incident radiant heat flux. Prompt fixation and measuring should be performed to minimize the contamination of dried insulation pads with atmospheric moisture.

Figure 8: Oven used to dry the insulation layers

- 45 %WME

A plastic box was filled with water up to 40 mm level and a stand was placed at the bottom, which stood above the water level. Insulation layers were kept inside the sealed container on the stand for 9-12 hours. Then the moisture level was measured using the thermal hygrometer. The insulation layers showed 45 %WME.

- 65 %WME

For this preparation, a plastic box is filled with water up to 40 mm. A horizontal platform was set just above the water level. The PT was placed on top of the platform and the box was sealed to allow saturation. The moisture level was monitored continuously until it reached about 65 %WME; this typically takes 24 hours to reach the desired moisture percentage.

- 98 %WME (comparable to a raining condition)

The insulation layers were prepared to imitate the environmental condition of the wet humid day by dropping several water droplets on the insulation layers. Then the moisture percentage was measured using the hygrometer and the reading was 98 %WME.

3.3 Calibration and Data Collection

The purpose of the calibration process is to determine a relationship between the measured surface temperature and the ideal surface temperature. These data can then be utilized to develop a correlation between the ideal surface temperature and the received heat flux. WCRM was used to measure the incident radiant heat flux under the cone calorimeter along with the PT. Objects under the cone calorimeter heater are generally exposed to both radiation heat from the cone heater and the convective heat from the surrounding gas. The contribution of convective heat transfer should be minimized to optimize the results' accuracy. According to previous studies, the maximum variation in the radiation heat flux on the center of the cone calorimeter is 2% in a horizontal orientation and 7% in the vertical orientation. The main reason behind this deviation in vertical orientation was identified as the availability of pronounced convective heat flux (Babrauskas & Parker, 1986). Therefore, the horizontal configuration was selected to arrange the calibration setup with

the WCRM and the PT aligning the middle of the frustum under the cone calorimeter heater. The PT and the WCRM were fixed close to each other as 50 mm and 25 mm under the center of the frustum, complying with ISO-5660 as in.

Figure 9: Experimental set up of Radiometer and PT under the cone calorimeter

The calibration was done by gradually increasing the temperature of the cone calorimeter (Fire Testing Technology). The cone calorimeter heater standing in the ambient temperature at the beginning of the test was heated up to 200^{o}C as the first step. This temperature was maintained for about 300 seconds at a constant to provide steady-state condition to the specimen before raising the temperature again by 100^{0}C. This process was continued until the cone calorimeter heater reached 900^{0}C. During the entire calibration process, the cone calorimeter delivered an incident radiant heat flux within the range of 0-75 kW/m^{2}. Since the Rayleigh number was less than 10^{3} the contribution of convection to the calibration process was considered negligible. When the Rayleigh number moves more than 10^{4}, the convection contribution becomes significant and the surface boundary layer gets thinner. (Sheikholeslami & Ganji, 2016) The two major contributors for this minimum convection are; the horizontal configuration and the new small size of the PT. During the entire calibration process, surfaces of the WCRM were cooled by cooling water. This

indeed ensured maintaining the environmental temperature on the surfaces of the WCRM, which then resulted in negligible convection from the surface to the environment. This ensures the environment as convection free, radiation only environment hence all components under the cone calorimeter can be considered as being exposed to the same incident radiant heat flux.

The PT heat balance equation for a steady-state mixed radiation/convection environment is shown in Eq. (18) below.

$$0 = \varepsilon_{PT}\dot{q}_{inc-rad} - \varepsilon_{PT}\sigma T_{s-ideal}^4 - h(T_{s-ideal} - T_g) \tag{18}$$

Considering the radiation only environment, Eq. (18) can be modified as Eq. (19)

$$\varepsilon_{PT}\dot{q}''_{inc-rad} - \varepsilon_{PT}\sigma T_{ideal}^4 = 0 \tag{19}$$

The incident heat flux values measured in the calibration process can be used to determine the corresponding ideal surface temperature values in a steady state. Using the calculated steady-state ideal surface temperature and measured surface temperature values, a relation can be developed between these two temperatures as in Eq. (20),

$$T_{ideal} = -(1.52E-4)T_{measured}^2 + 1.22T_{measured} - 58.3 \tag{20}$$

$$\dot{q}''_{inc-rad} = \frac{\rho c_p \delta \frac{dT_{s-ideal}}{dt} + \varepsilon_{PT}\sigma T_{s-ideal}^4}{\varepsilon_{PT}} \tag{21}$$

In a radiation only environment, by combining Eq. (14) and Eq. (18), a unique equation for incident radiant heat flux can be derived as following Eq. (21).

The PTs representing all the scenarios; unheated, preheated, 0, 45, 65, and 98 %WME were tested under the cone calorimeter heater in the same manner to measure the metal surface

temperatures of the PT. Using the equation above, incident radiant heat flux was calculated from the measured surface temperatures.

CHAPTER IV

RESULTS & ANALYSIS

4.1. Analysis of Experimental Results

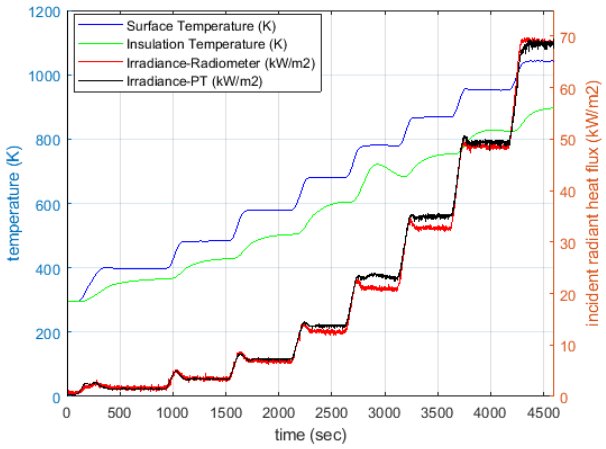

Figure 10: Temperature and heat flux readings from unheated PT

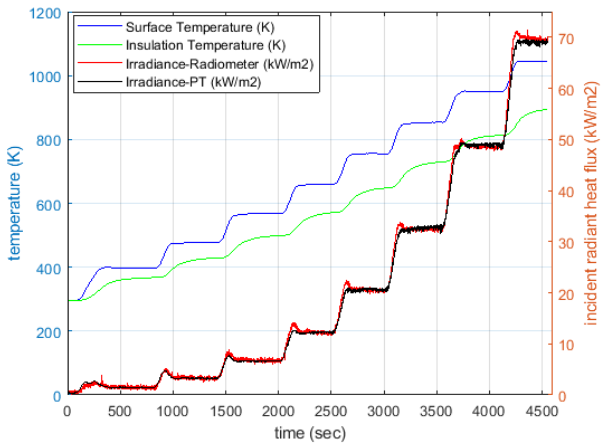

Figure 11: Temperature and heat flux readings from preheated PT

Changes of temperature and incident radiant heat flux of the unheated PT and preheated PT are shown in Figure 10 and Figure 11 respectively. The starting moisture percentage of the unheated PT was 15% while the preheated PT had approximately 5% moisture.

The insulation layer of unheated PT exhibited an abrupt change upon the temperature of the cone calorimeter reaching 600^{o}C (approximately 2800 sec - 3200 sec). Incident radiant heat flux from PT showed a higher value than the WCRM in the range of that abrupt change. The gap of measurements was conjectured as the amount of heat required to break the internal bonds of the fresh ceramic fiber insulation layers.

In the preheated PT, the surface and the insulation layer temperatures increased without any noticeable deviation with the increment of cone heater temperature. The main reason for these consistent temperature readings was that the PT has been used previously and the internal microphysical bonds have already been broken. As a result, no further heat was required to break these internal bonds. That makes the measured incident radiant heat flux calculated by the PT match with that from WCRM. Further, this proves the calculations of the incident radiant heat flux of preheated PT have high accuracy than the unheated PT.

Temperature and incident radiant heat flux fluctuations with %WME: 0, 45, 65, and 98 are shown in Figure 12, Figure 13, Figure 14 and Figure 15 respectively. Respective Moisture content for the %WME in the PT insulation layers can be calculated from Eq. (10). The range of densities of woods is in between 0.320 g/cm^3 to 0.720 g/cm^3. Hence, 0.520 g/cm^3 was considered as the average value for the calculations as shown in Table 3 below.

Table 3: conversion of the %WME to the moisture content of ceramic fiber

WME percentage	Moisture content percentage in ceramic fiber
0	0
45	87
65	125
98	188

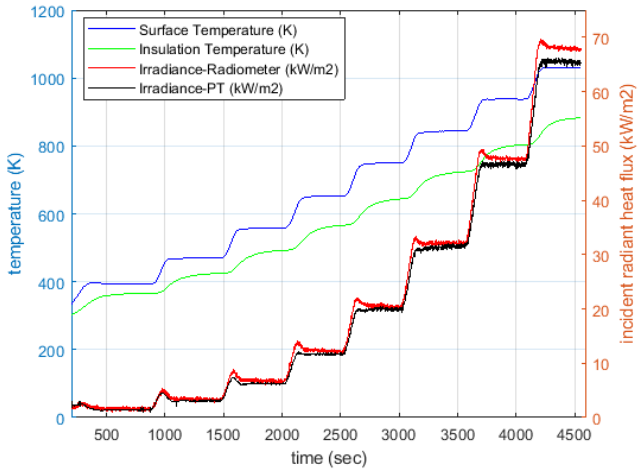

Figure 12: Experiment results for 0 %WME

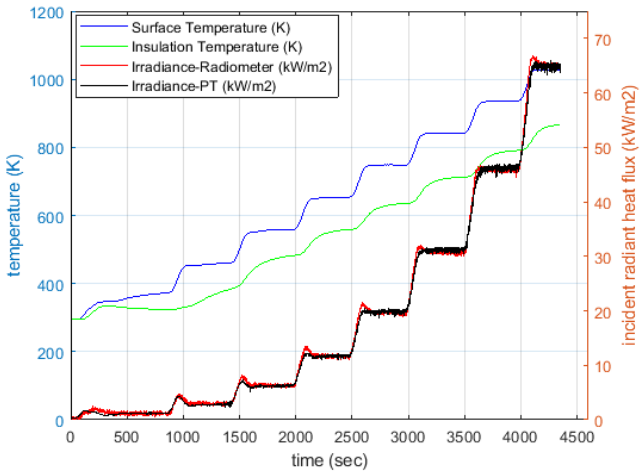

Figure 13: Experiment results for 45 %WME

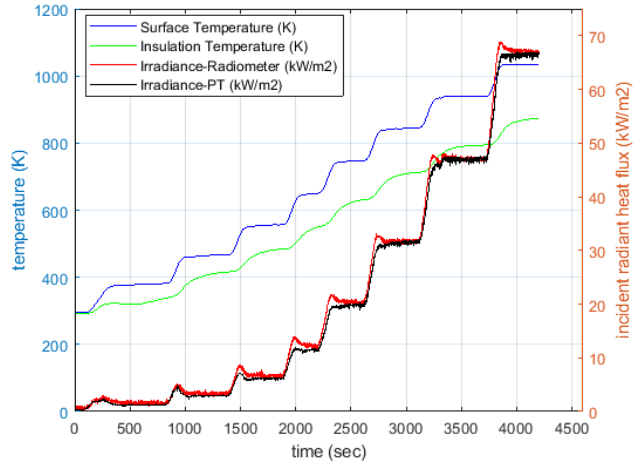

Figure 14: Experiment results for 65 %WME

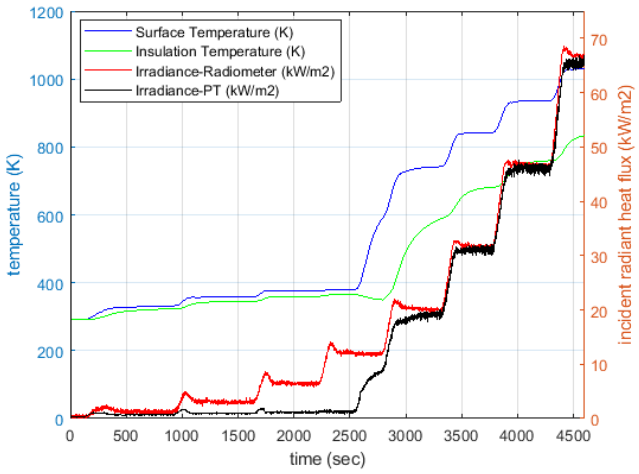

Figure 15: Experiment results for 98 %WME

Graphs for moisture 0, 45, and 65 %WME show comparatively similar trends in the sense of temperature and the incident radiant heat flux. Both metal surface and insulation layer temperatures increase with the cone heater temperature without exhibiting any abnormalities. On the contrary, for 98 %WME in Figure 15, temperature reading of the Inconel alloy plate and the insulation layer is very close within the first 2700 seconds. This observation agrees with Kočí, who suggested that the moisture acts as a better thermal conductor. When the insulation has more moisture inside, the heat gradient will be less due to high heat flow throughout the insulation until adequate moisture exists.

To explain this phenomenon further, a comparison between the average incident radiant heat flux from WCRM and PT is shown in Table 4 below.

Table 4: Average incident radiant heat flux values for 0, 45, 65, and 98 %WME in steady state

Cone T. (°C)	0 %WME			45 %WME			65 %WME			98 %WME		
	Average incident radiant heat flux (kW/m^2)											
	WCRM	PT	Error %	WCRM	PT	Error %	WCRM	PT	Error %	WCRM	PT	Error %

200	1.47	1.48	**11.77**	1.16	1.17	**0.89**	1.60	1.26	**21.02**	1.23	0.69	**43.73**
300	3.36	3.08	**8.41**	2.95	2.79	**5.44**	3.34	2.97	**11.18**	3.03	0.96	**68.17**
400	6.76	6.26	**7.26**	6.28	6.22	**1.04**	6.76	6.13	**9.25**	6.44	1.16	**82.05**
500	12.31	11.68	**5.15**	11.67	11.68	**0.03**	12.35	11.44	**7.34**	12.00	4.35	**63.75**
600	20.53	19.95	**2.83**	19.93	19.84	**1.07**	20.51	19.68	**4.04**	20.17	18.90	**6.33**
700	32.11	31.44	**2.11**	30.71	31.19	**1.55**	31.71	31.36	**1.11**	31.82	31.07	**2.36**
800	47.72	46.59	**2.36**	45.73	46.20	**1.02**	47.11	46.96	**0.31**	46.78	46.13	**1.38**
900	68.04	65.51	**3.72**	65.36	64.93	**0.65**	67.19	66.40	**1.18**	66.67	65.56	**1.67**

The above table shows approximately similar average incident radiant heat flux values in 0, 45, and 65 %WME. The percentage error in small incident heat flux values ($< 10 \frac{kW}{m^2}$) is relatively larger than that of higher heat flux range, especially for 0 and 65 %WME. But when observed closely, even though the percentage error is relatively high, the maximum difference between the incident radiant heat flux values can be calculated as 0.63 $\frac{kW}{m^2}$ for the above mentioned range. Even the value difference is small, in small measuring heat flux values; it could give relatively high percentage error values as Eq. (22) follows.

$$error[\%] = abs(\frac{\dot{q}''_{inc-rad-WCRM} - \dot{q}''_{inc-rad-PT}}{\dot{q}''_{inc-rad-WCRM}}) \times 100 \quad (22)$$

The main possible reason for this small percentage error incorporate with 0, 45, and 65 %WME is the uncertainties associated with WCRMs as explained in the above section. Further, the higher percentage error associates with the 98 %WME for cone temperature level less than 500^{o}C can be explained with the use of Table 5 below.

Considering the Incident radiant heat flux value of the WCRM as a reference, the heat difference between the WCRM and PT was calculated. Incident radiant heat flux and heat values for the aforementioned %WME are tabulated in Table 5 below.

Table 5: Details of moisture content and vaporization energy (0, 45, 65, and 98 %WME)

%WME	Mass of moisture (g)	Energy to vaporized moisture from PT (kJ)	Calculated heat (difference of WCRM and PT (kJ))	% Error between calculated and measured incident radiant heat flux
0	0.00	0.00	0.97	7.5
45	0.96	2.48	0.28	9.6
65	1.40	3.58	1.10	9.6
98	2.10	5.40	7.01	51.5

Calculated heat from WCRM and PT was much lower than the required heat to evaporate moisture content from the PT insulation layers for 0, 45, and 65 %WME. Additionally, incident radiant heat flux values from Table 4 prove the negligible amount of heat allocated by PT to vaporize the moisture inside. However, it was obvious that the moisture could not withstand the temperatures above 100^{o}C. There could be limited possible reasons to resolve this conflict, which are explained below.

Since the comparatively less mass of moisture available in the PT, there could be a high chance that the wool blanket wrapped around the PT could absorb moisture from the insulation layer. As the wool blanket exposed to the thermal environment, the inside moisture content also reduced drastically with the high temperature. These void spaces would allow moisture to transfer from insulation to wool blanket. In a practical situation, there could be some loose points where the mechanical wire that ties the wool blanket was

not tight enough to block the surface. This helps moisture to evaporate from the insulation layer without getting any additional heat from the plate and not changing the calculated incident radiant heat flux from the measured value.

In addition to that, the incident radiant heat flux readings of the WCRM in the moisture level 98 %WME is noticeably higher than that of the PT. The main reason for this considerable amount of incident radiant heat flux difference is considered as the evaporation heat absorbed by water. The evaporation heat required and measured heat from the experiment listed in Table 5 above. The difference between the incident radiant heat flux of WCRM and PT is found to be approximately similar to the energy needed for the evaporation (Appendix C). The incident radiant heat flux showed a value different until the cone calorimeter heater temperature became 500^{o}C (approximately 2700 seconds in Figure 15). Moisture inside the insulation layers took the exact time to evaporate according to the graph and the calculations. After moisture evaporated during the first 2700 seconds, incident radiant heat fluxes were observed to be the same, which illustrates no heat was allocated to vaporized moisture, as there was no more moisture left. This shows the incident radiant heat flux calculations done using the PT with high moisture levels as 98 %WME, are not accurate in low-temperature environments (below 700^{o}C, 30 kW/m^{2}).

The highest %EMC observed under the maximum possible weather condition of 100% RH lies in between 27 to 30 percent as in Figure 5, which is well below for all 45, 65, and 98 %WME. The calculated moisture content percentage from Eq. (10) proves that all considered moisture levels contain more moisture than it should be in 100% RH. In addition to that, 98 %WME represents high moisture percentage as 188, which elaborates on the real environmental conditions on a possible rainy day. As this was gained by

dropping water droplets onto the PT insulation layer, it consists of more water than the EMC. This phenomenon demands the PT to allocate more heat to vaporize the water inside and gives low readings for incident radiant heat flux, which is less accurate. This analysis proves that even with more moisture content inside, PT would give accurate enough temperature readings to calculate incident radiant heat flux given that no water droplets inside the PT, as a rainy day.

To calculate the incident heat flux in both radiation only and mixed radiation/ convection environments, the researchers developed a spreadsheet program using the ideal surface temperature correlations. The interface of the developed program is shown in Figure 16 and Figure 17.

R5

	A	B	C	D	E	F	G	H	I	J	K	L	M	N	O
1	Time-One Time Used	PT Temperature (K)	Radiometer (mV)-One Time Used		Radiometer (kW/m2)-One Time Used	calculted Ideal Surface T. (K)-from equation	calculted Ideal Surface T. (K)-from corelation	calculted Ideal Surface T. (K)-from corelation (7pt average)		cone T(oC)	OneTime Used-steady state time period	metal surface T(K) average	Radiometer reading (kW/m2)	calculated IST from equation (K) average	IST from corelation (K) OneTime used
2	**0**	**296.78**	0.04		0.45	298.78	298.78	298.78		200	500-800	397.10	1.47	400.09	402.65
3	**1**	**296.78**	0.03		0.38	285.51	290.66	296.08		300	1100-1400	477.46	3.31	491.25	490.17
4	**2**	**296.79**	0.04		0.45	298.78	298.78	307.62		400	1700-2000	567.74	6.76	587.64	586.19
5	**3**	**296.79**	0.07		0.75	339.38	339.38	306.15		500	2200-2500	659.63	12.27	682.08	681.43
6	**4**	**296.79**	0.05		0.53	310.49	310.49	306.15		600	2700-3000	755.01	20.53	775.68	777.58
7	**5**	**296.78**	0.04		0.45	298.78	298.78	307.50		700	3200-3500	851.81	32.44	869.72	872.39
8	**6**	**296.78**	0.04		0.45	298.78	298.78	306.15		800	3800-4100	950.44	48.56	962.00	966.10
9	**7**	**296.78**	0.04		0.45	298.78	298.78	299.38		900	4250-4550	1044.57	69.86	1053.56	1052.80
10	**8**	**296.78**	0.01		0.15	227.36	290.66	302.73							
11	**9**	**296.77**	0.04		0.45	298.78	298.78	301.37		**radiometer corelation with kW and mV**					
12	**10**	**296.78**	0.06		0.68	330.58	330.58	310.77			kW=	0	mV^2	11.42	mV
13	**11**	**296.78**	0.03		0.38	285.51	290.66	312.73							
14	**12**	**296.78**	0.08		0.90	355.19	355.19	319.38		**Corelation between ideal and measured surface temperatures**					
15	**13**	**296.78**	0.05		0.53	310.49	310.49	326.15		IST=		measured^3	-1.50E-04	measured^2	1.2204
16	**14**	**296.77**	0.06		0.68	330.58	330.58	320.85							
17	**15**	**296.77**	0.07		0.75	339.38	339.38	325.90							
18	**16**	**296.76**	0.04		0.45	298.78	298.78	320.21							
19	**17**	**296.78**	0.05		0.60	321.01	321.01	326.39							
20	**18**	**296.77**	0.05		0.60	321.01	321.01	329.21							
21	**19**	**296.77**	0.07		0.83	347.55	347.55	330.58							
22	**20**	**296.77**	0.07		0.83	347.55	347.55	338.70							
23	**21**	**296.78**	0.07		0.83	347.55	347.55	335.00							
24	**22**	**296.76**	0.07		0.83	347.55	347.55	335.00							
25	**23**	**296.78**	0.04		0.45	298.78	298.78	326.87							
26	**24**	**296.78**	0.05		0.60	321.01	321.01	325.51							

Figure 16: (a) interface of the incident heat flux calculation program (calibration)

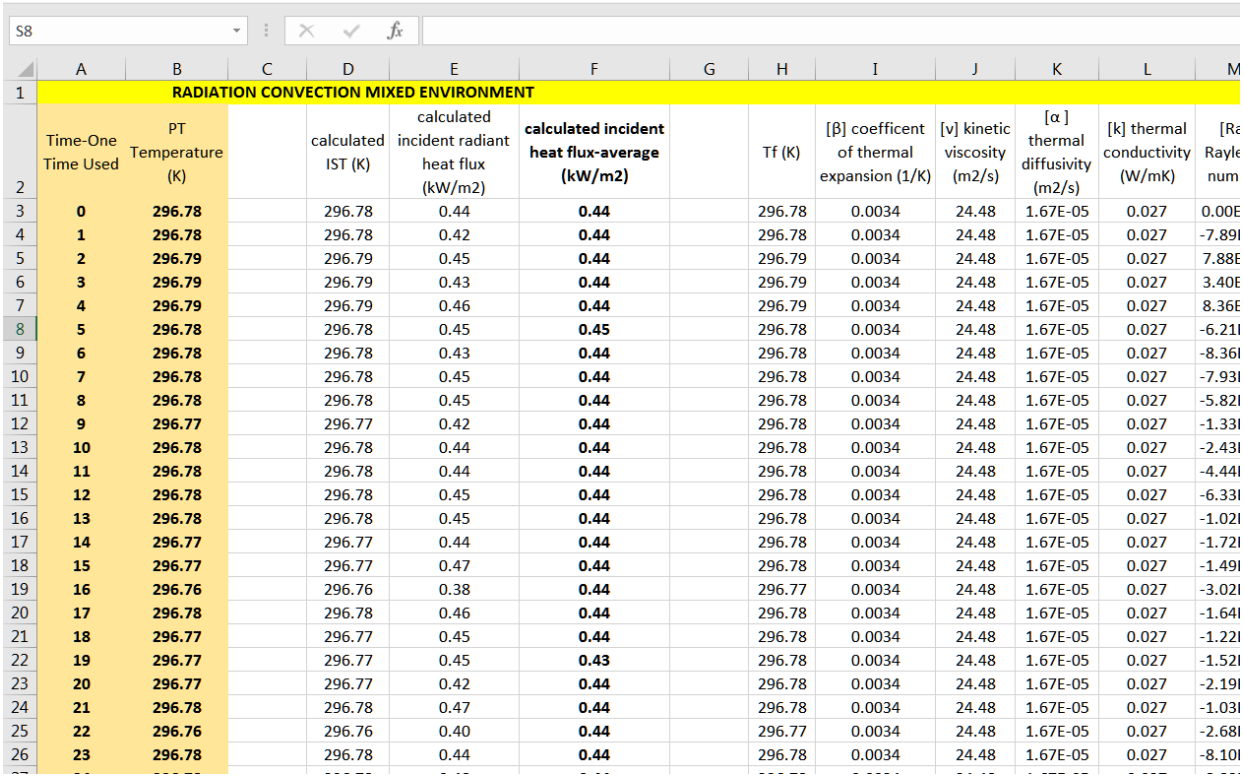

	A	B	C	D	E	F	G	H	I	J	K	L	M
1	RADIATION CONVECTION MIXED ENVIRONMENT												
2	Time-One Time Used	PT Temperature (K)		calculated IST (K)	calculated incident radiant heat flux (kW/m2)	**calculated incident heat flux-average (kW/m2)**		Tf (K)	[β] coefficent of thermal expansion (1/K)	[v] kinetic viscosity (m2/s)	[α] thermal diffusivity (m2/s)	[k] thermal conductivity (W/mK)	[Ra Rayle num
3	**0**	**296.78**		296.78	0.44	**0.44**		296.78	0.0034	24.48	1.67E-05	0.027	0.00E
4	**1**	**296.78**		296.78	0.42	**0.44**		296.78	0.0034	24.48	1.67E-05	0.027	-7.89I
5	**2**	**296.79**		296.79	0.45	**0.44**		296.79	0.0034	24.48	1.67E-05	0.027	7.88E
6	**3**	**296.79**		296.79	0.43	**0.44**		296.79	0.0034	24.48	1.67E-05	0.027	3.40E
7	**4**	**296.79**		296.79	0.46	**0.44**		296.79	0.0034	24.48	1.67E-05	0.027	8.36E
8	**5**	**296.78**		296.78	0.45	**0.45**		296.78	0.0034	24.48	1.67E-05	0.027	-6.21I
9	**6**	**296.78**		296.78	0.43	**0.44**		296.78	0.0034	24.48	1.67E-05	0.027	-8.36I
10	**7**	**296.78**		296.78	0.45	**0.44**		296.78	0.0034	24.48	1.67E-05	0.027	-7.93I
11	**8**	**296.78**		296.78	0.45	**0.44**		296.78	0.0034	24.48	1.67E-05	0.027	-5.82I
12	**9**	**296.77**		296.77	0.42	**0.44**		296.78	0.0034	24.48	1.67E-05	0.027	-1.33I
13	**10**	**296.78**		296.78	0.44	**0.44**		296.78	0.0034	24.48	1.67E-05	0.027	-2.43I
14	**11**	**296.78**		296.78	0.44	**0.44**		296.78	0.0034	24.48	1.67E-05	0.027	-4.44I
15	**12**	**296.78**		296.78	0.45	**0.44**		296.78	0.0034	24.48	1.67E-05	0.027	-6.33I
16	**13**	**296.78**		296.78	0.45	**0.44**		296.78	0.0034	24.48	1.67E-05	0.027	-1.02I
17	**14**	**296.77**		296.77	0.44	**0.44**		296.78	0.0034	24.48	1.67E-05	0.027	-1.72I
18	**15**	**296.77**		296.77	0.47	**0.44**		296.78	0.0034	24.48	1.67E-05	0.027	-1.49I
19	**16**	**296.76**		296.76	0.38	**0.44**		296.77	0.0034	24.48	1.67E-05	0.027	-3.02I
20	**17**	**296.78**		296.78	0.46	**0.44**		296.78	0.0034	24.48	1.67E-05	0.027	-1.64I
21	**18**	**296.77**		296.77	0.45	**0.44**		296.78	0.0034	24.48	1.67E-05	0.027	-1.22I
22	**19**	**296.77**		296.77	0.45	**0.43**		296.78	0.0034	24.48	1.67E-05	0.027	-1.52I
23	**20**	**296.77**		296.77	0.42	**0.44**		296.78	0.0034	24.48	1.67E-05	0.027	-2.19I
24	**21**	**296.78**		296.78	0.47	**0.44**		296.78	0.0034	24.48	1.67E-05	0.027	-1.03I
25	**22**	**296.76**		296.76	0.40	**0.44**		296.77	0.0034	24.48	1.67E-05	0.027	-2.68I
26	**23**	**296.78**		296.78	0.44	**0.44**		296.78	0.0034	24.48	1.67E-05	0.027	-8.10I

Figure 17: (b) interface of the incident heat flux calculation program

CHAPTER V

CONCLUSION

The purposes of the current study are to investigate the effect of moisture content in the PT insulation on the measurement of incident radiant heat flux and to investigate the effect of preheating of PT on the measurement accuracy of the incident radiant heat flux. To compare the heat flux measurements, the study was conducted in two phases; (i.) unheated PT against preheated PT, (ii.) different moisture levels inside the PT. The incident radiant heat fluxes received by PT under different conditions was evaluated. WCRM was attached to all tests with PT and the unit was tested under the cone calorimeter. The equation used to calculate the incident radiant heat flux has been developed using the ideal surface temperature method. As the first phase of the study, an unheated PT was tested against a preheated PT. In this test, the calibration equation was developed using the preheated PT. The results using this calibration equation show that the preheated PT provided comparatively accurate enough results than the unheated PT. The second phase of the study was to compare the calculated incident radiant heat fluxes from PTs with different %WME. Four moisture contents were studied equivalent to 0, 45, 65, and 98 %WME. All %WME

were converted to actual moisture content inside the PT by using a correlation. Considering the relationship between RH and %WME, the values of 40, 65, 98 %WME were deemed to contain more moisture than the equilibrium with a 100% RH. The findings of this study showed that the incident radiant heat fluxes calculated using PT of 0 to 65 %WME did not deliver any noteworthy difference with that from the WCRM. A factor that might have supported this under-represented difference is explained descriptively in the results and analysis section. The evaporation of moisture from the PT with 98 %WME is accountable for the difference between the calculated and measured heat fluxes. To conclude, the researchers recommend the use of a preheated PT with any weather conditions. for accurate enough incident radiant heat flux measurement given that no water droplets have been poured into the PT.

REFERENCES

Ahmed, M. Z. (2006). *EVALUATION OF MOISTURE CONTENT IN WOOD FIBER AND RECOMMENDATION OF THE BEST METHOD FOR ITS DETERMINATION*. 127.

Arther, M., & Saffer, D. (2015). *Relative Humidity | EARTH 111: Water: Science and Society*. https://www.e-education.psu.edu/earth111/node/557

ASTM E3057-19. (2019). *Standard Test Method for Measuring Heat Flux Using Directional Flame Thermometers with Advanced Data Analysis Techniques*. https://www.astm.org/Standards/E3057.htm

Babrauskas, V., & Parker, W. J. (1986). *Ignitability measurements with the cone calorimeter*. National Bureau of Standards. http://archive.org/details/ignitabilitymeas8634babr

Bahrami, M. (2013). *First Law of Thermodynamics_Closed Systems.pdf*. https://www.sfu.ca/~mbahrami/ENSC%20388/Notes/First%20Law%20of%20Thermodynamics_Closed%20Systems.pdf

Condensation Fact Sheet. (2019). Condensation Fact Sheet. *Metal Building Manufacturers Association*, 5.

Cone calorimeter. (2019). *Cone calorometer (ISO 5660 ASTM E 1354)*. http://www.tech-quality.com/images/pdf/FTT/cone.pdf

Govett, R., Mace, T., & Bowe, S. (2019). *BiomassMoistureContent.pdf*. https://dnr.wi.gov/topic/ForestBusinesses/documents/BiomassMoistureContent.pdf

Häggkvist, A. (2009). *The Plate Thermometer as a Mean of Calculating Incident Heat Radiation*. 96.

Häggkvist, A., Sjöström, J., & Wickström, U. (2013). Using plate thermometer measurements to calculate incident heat radiation. *Journal of Fire Sciences*, *31*(2), 166–177. https://doi.org/10.1177/0734904112459264

Hailwood, A. J., & Horrobin, S. (1946). Absorption of water by polymers: Analysis in terms of a simple model. *Transactions of the Faraday Society*, *42*(0), B084–B092. https://doi.org/10.1039/TF946420B084

Hedlin, P. (1988). *Heat flow through a roof insulation having moisture contents between 0 and 1% by volume in summer*. http://web.mit.edu/parmstr/Public/NRCan/nrcc31111.pdf

Hukseflux SBG01 user manual v1208. (2011). *Water cooled heat flux sensor according to Schmidt Boelter, User manual*. http://au.ictinternational.com/content/uploads/2014/06/SBG01-manual-v1208.pdf

Hurley, M. J. (2016). *SFPE Handbook of Fire Protection Engineering, 5th Edition—SFPE*. https://www.sfpe.org/page/Handbook5thEdition

Ingason, H., & Wickström, U. (2007). Measuring incident radiant heat flux using the plate thermometer. *Fire Safety Journal*, *42*(2), 161–166. https://doi.org/10.1016/j.firesaf.2006.08.008

Introduction to moisture content determination, Purdue University. (2019). https://engineering.purdue.edu/~abe305/moisture/html/page6.htm

Kang, S., Kwon, M., Choi, J. Y., & Choi, S. (2019). Thermal Boundaries in Cone Calorimetry Testing. *Coatings*, *9*(10), https://www.mdpi.com/2079-6412/9/10/629. https://doi.org/10.3390/coatings9100629

Kočí, V., Vejmelková, E., Čáchová, M., Koňáková, D., Keppert, M., Maděra, J., & Černý, R. (2017). Effect of Moisture Content on Thermal Properties of Porous Building Materials. *International Journal of Thermophysics*, *38*(2), 1–12. https://doi.org/10.1007/s10765-016-2164-8

Kourtides, D. A., Pitts, W. C., Araujo, M., & Zimmerman, R. S. (1988). High-Temperature Properties of Ceramic Fibers and Insulations for Thermal Protection of Atmospheric Entry and Hypersonic Cruise Vehicles. *Journal of Fire Sciences*, *6*(5), 313–332. https://doi.org/10.1177/073490418800600501

Lawrence, M. G. (2005). The Relationship between Relative Humidity and the Dewpoint Temperature in Moist Air: A Simple Conversion and Applications. *Bulletin of the American Meteorological Society*, *86*(2), 225–234. https://doi.org/10.1175/BAMS-86-2-225

LEARN London Metroplitan University. (2004). *Thermal Conductivity*. https://www.new-learn.info/packages/clear/thermal/buildings/building_fabric/properties/conductivity.html

Mitchell, P. (2017). *Calculating the Equilibrium Moisture Content – Wood Products Extension*. https://research.cnr.ncsu.edu/blogs/wpe/2017/11/17/calculating-the-equilibrium-moisture-content/

Mitchell, P. H. (2017). Calculating the Equilibrium Moisture Content for Wood Based on Humidity Measurements. *BioResources*, *13*(1), 171–175. https://doi.org/10.15376/biores.13.1.171-175

Mohammed, I., Talib, A. R. A., Sultan, M. T. H., & Saadon, S. (2016). Temperature and heat flux measurement techniques for aeroengine fire test: A review. *IOP Conference Series: Materials Science and Engineering*, *152*, 012036. https://doi.org/10.1088/1757-899X/152/1/012036

Nakos. (2010). *Description of heat flux measurement methods used in Hydrocarbon and propellant fuel fires at Sandia*. http://www.techno-office.com/file/MED_19.pdf

Nakos, J. T. (2005). *Uncertainty analysis of steady state incident heat flux measurements in hydrocarbon fuel fires.* (No. SAND2005-7144, 876525; pp. SAND2005-7144, 876525). https://doi.org/10.2172/876525

NFPA 921 (2011). (2013). https://www.nfpa.org/Assets/files/AboutTheCodes/921/921_F2013_FIA-AAA_SDReport.pdf

Ochs, R. I., Kao, Y.-H., Tambe, S. B., & Jeng, S.-M. (2013, December 5). *The Uncertainty of Temperature and Heat Flux Calibration for FAA Fire Test*. 7th International Fire & Cabin Safety Research Technical Conference.

OMEGA user's guide. (2019). *M5506.pdf*. https://assets.omega.com/manuals/M5506.pdf

Robertson, A. F., & Ohlemiller, T. J. (1995). *Low Heat-flux Measurements: Some Precautions*. https://doi.org/10.1016/0379-7112(95)00036-4

Sheikholeslami, M., & Ganji, D. D. (2016). *Koci*. https://www.sciencedirect.com/topics/chemistry/rayleigh-number/pdf

Shen, R., Park, H., Liu, Q., & Wanq, Q. (2019). *A new method to calculate adiabatic surface temperature using plate thermometer in an ambient condition | Elsevier Enhanced Reader*. https://doi.org/10.1016/j.applthermaleng.2018.12.021

Simpson, W. T. (1998). *Equilibrium moisture content of wood in outdoor locations in the United States and worldwide* (FPL-RN-268; p. FPL-RN-268). U.S. Department of Agriculture, Forest Service, Forest Products Laboratory. https://doi.org/10.2737/FPL-RN-268

Sun, J., Hu, Z., Zhuo, J., Wang, X., & Sun, C. (2014). *Thermal properties of highly porous fibrous ceramics*. 5.

Thermal ceramics. (2019). *Kaowool-Low-Temp-Boards.pdf*. https://www.fabricationspecialties.com/pdf/lowtemp.pdf

UC Merced Engineering. (2002). *Determining the moisture content of soil (conventional oven method)*. https://eng.ucmerced.edu/snsjho/files/MHWG/Laboratory/Soils/Protocol/Chapter_3_Moisture_content.pdf

APPENDICES

APPENDIX A

*** Calculate %WME to moisture content percentage of generic concrete using dry basis moisture content method.**

$$MC\% = \frac{\rho_{wood}}{\rho_{material}} WME\%$$

where,

ρ_{wood} = *density of wood highest* [0.72 g/cm^3]

$\rho_{concrete}$ = *density of concrete highest* [2.40 g/cm^3]

Calculated values of the moisture content percentage of generic concrete using the dry method and %WME are shown in the figure below. Reference values for the moisture content percentage for generic concrete are taken from Table 1

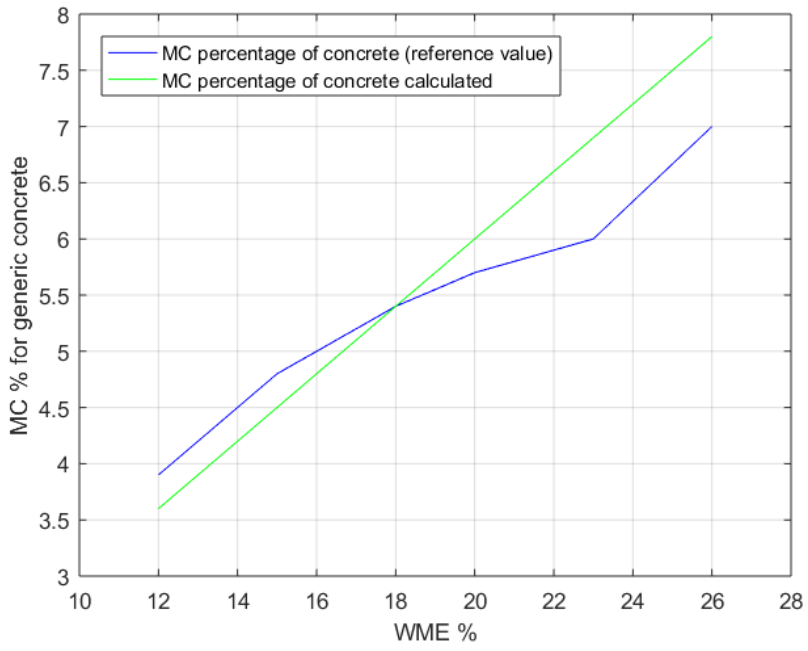

Figure 18: Regenerating moisture content percentage values for generic concrete using %WME and dry moisture content method

APPENDIX B

*** Calculation of Biot number**

$$Bi = \frac{h_c L}{k}$$

Assuming $\frac{W}{mK} = 20\frac{W}{m^2 K}$, $k = 14\frac{W}{mK}$ at 298K

$$Bi = \frac{20 * 0.000584}{14} = 0.000727 < 0.1$$

Since the Biot number<0.1 based on the calculations above, the lumped thermal approximation of PT should be valid in our experiment.

APPENDIX C

*** Calculation of moisture vaporization energy (required)**

$$Heat_{vap} = Heat_{100^oC} + Heat_L$$
$$= mc\theta + mL_v$$

where,

$m = mass\ of\ moisture\ [g]$

$c = specific\ heat\ capacity\ of\ water\ [J/gK]$

$\theta = temperature\ difference\ [K]$

$L_v = latent\ heat\ [J/g]$

Considering 98 *percent moisture content, water mass is* 2.1 *g*

$$Heat_{vap} = 2.1g * [4.2J/g.K * (100-22)K + 226J/g]$$
$$= 5433\ J$$

Considering 65 *percent moisture content, water mass is* 1.4 *g*

$$Heat_{vap} = 1.4g * [4.2J/g.K * (100-22)K + 226J/g]$$
$$= 3622\ J$$

Calculate heat different between radiometer and PT

- *Used trapezoidal method to calculate the area under the heat flux curves*
- *The area between the curves of WCRM and PT considered as the heat required vaporizing the moisture content inside the insulation.*
- *Area of the PT* $= 6.5x10^{-4} m^2 (0.0254m\ x\ 0.0254m)$

98 WME,

heat different between WCRM and the PT $= 7.01\ kW/m^2$

65 WME,

heat different between WCRM and the PT $= 1.10\ kW/m^2$

VITA

Lahiru Jayathunga Mudiyanselage

Candidate for the Degree of

Master of Science

Thesis: EFFECT OF MOISTURE LEVEL IN PLATE THERMOMETER INSULATION ON THE MEASUREMENT OF INCIDENT RADIANT HEAT FLUX

Major Field: Fire Safety and Explosion Protection

Biographical:

Education:

Completed the requirements for the Master of Science in Fire Safety and Explosion Protection at Oklahoma State University, Stillwater, Oklahoma in May 2020

Completed the requirements for the Bachelor of Science in Mechanical Engineering at University of Moratuwa, Colombo, Sri Lanka in 2013.

Experience:

Graduate Teaching Assistant at Engineering Technology, Oklahoma State University, Stillwater, Oklahoma (August 2019-May 2020)

Professional Memberships:

Associate Member of the Institute of Engineers in Sri Lanka since 2013.